



# Effect of geometry on dielectrophoretic trap stiffness in microparticle trapping

Mohammad Rizwen Ur Rahman<sup>1</sup> · Tae Joon Kwak<sup>2</sup> · Jörg C. Woehl<sup>3</sup> · Woo-Jin Chang<sup>1,4</sup>

Accepted: 11 June 2021 / Published online: 29 June 2021

© The Author(s), under exclusive licence to Springer Science+Business Media, LLC, part of Springer Nature 2021

## Abstract

Dielectrophoresis, an electrokinetic technique, can be used for contactless manipulation of micro- and nano-size particles suspended in a fluid. We present a 3-D microfluidic DEP device with an orthogonal electrode configuration that uses negative dielectrophoresis to trap spherical polystyrene micro-particles. Traps with three different basic geometric shapes, i.e. triangular, square, and circular, and a fixed trap area of around  $900 \mu\text{m}^2$  were investigated to determine the effect of trap shape on dynamics and strength of particle trapping. Effects of trap geometry were quantitatively investigated by means of trap stiffness, with applied electric potentials from  $6 V_{\text{P-P}}$  to  $10 V_{\text{P-P}}$  at 1 MHz. Analyzing the trap stiffness with a trapped  $4.42 \mu\text{m}$  spherical particle showed that the triangular trap is the strongest, while the square shape trap is the weakest. The trap stiffness grew more than eight times in triangular traps and six times in both square and circular traps when the potential of the applied electric field was increased from  $6 V_{\text{P-P}}$  to  $10 V_{\text{P-P}}$  at 1 MHz. With the maximum applied potential, i.e.  $10 V_{\text{P-P}}$  at 1 MHz, the stiffness of the triangular trap was 60% and 26% stronger than the square and circular trap, respectively. A finite element model of the microfluidic DEP device was developed to numerically compute the DEP force for these trap shapes. The findings from the numerical computation demonstrate good agreement with the experimental analysis. The analysis of three different trap shapes provides important insights to predict trapping location, strength of the trapping zone, and optimized geometry for high throughput particle trapping.

**Keywords** Dielectrophoresis · Trap geometry · Trap stiffness · Microfluidic device · Microparticle trapping

## 1 Introduction

Ever since Herbert Pohl and Ira Hawk (Pohl and Hawk 1966) demonstrated the separation of live from dead yeast cells using dielectrophoresis (DEP), a significant number of theoretical and experimental studies have been carried out based upon this discovery to control and manipulate micro- and nanoparticles movements. DEP is the electrokinetic movement of polarizable particles suspended in a fluid

medium under the influence of a non-uniform electric field. Compared to other electric field-driven particle separation techniques, DEP does not require the particle to be charged, but relies on the separation of intrinsic charge within the particle to generate an induced dipole that depends on the relative polarizability of the particle and its surrounding medium (Pethig 2010a). Based on the relative polarizability of the particles compared to the surrounding medium, particles can be pulled towards the regions of higher electric field gradient or pushed from these regions (Mauro 1980; Pohl 1978). The phenomenon of attracting the particles to the regions of higher electric field gradient from the lower electric field regions is known as the positive DEP (p-DEP) and vice versa for negative DEP (n-DEP). As DEP allows particle separation based on their physical properties (such as size, shape) and structural properties (such as homogeneity, dielectric properties), it has been widely used in various label-free, contactless applications such as particle concentration and isolation (Dash and Mohanty 2014; Kwak et al. 2021, 2019b; Nejad et al. 2013), cell enrichment, sorting

✉ Woo-Jin Chang  
wjchang@uwm.edu

<sup>1</sup> Department of Mechanical Engineering, University of Wisconsin-Milwaukee, Milwaukee, WI 53211, USA

<sup>2</sup> Center for Systems Biology, Massachusetts General Hospital, Boston, MA 02114, USA

<sup>3</sup> Department of Chemistry and Biochemistry, University of Wisconsin-Milwaukee, Milwaukee, WI 53211, USA

<sup>4</sup> School of Freshwater Sciences, University of Wisconsin-Milwaukee, Milwaukee, WI 53204, USA

and separation (Becker et al. 1995; Huang et al. 2002; Lee et al. 2013b; Punjiya et al. 2019; Yang et al. 1999), medical diagnostics (Adekanmbi and Srivastava 2019; Park et al. 2015) and drug screening (Hoettges et al. 2008; Ivanoff et al. 2012; Pethig 2013).

For manipulation of micro- and nanoparticles suspended in various liquid media, it is desirable to develop microfluidic devices as they involve almost no moving parts. Microfluidic devices require a small volume of fluid and provide a large ratio of surface area to volume, which provides an opportunity for suspended particles to interact with the large surface area of the electrodes. Over the past decades, several methods have been demonstrated to manipulate and isolate the micro- and nano-sized particles using various microfluidic platforms. These approaches include optical-based separation (Ashkin et al. 1987; Hansen et al. 2005; Malagnino et al. 2002), hydrodynamic separation (Aragay et al. 2011; Chen et al. 2010; Dittrich and Manz 2006), mechanical filtration (D'Amico et al. 2017; Davies et al. 2012; Glazier and Arnold 1991; Lilliehorn et al. 2005), magnetic separation (Chen et al. 2013; Kollmannsberger and Fabry 2007; Winkleman et al. 2004), and dielectrophoretic manipulation (Castellanos et al. 2003; Chan et al. 1997; Sridharan et al. 2011). These active and passive particle separation methods were employed in micro- and nanoparticles controlling, trapping, focusing, separating, and characterizing applications. The optical particle separation methods, e.g. optical tweezers, typically require a high-power laser to exert forces on dielectric particles (Almendarez-Rangel et al. 2018; Pesce et al. 2015). The optical sources are expensive and require very sensitive measurements as well as extensive and careful calibration. Particle separation using magnetic force manipulates magnetic particles or magnetically tagged particles using magnetic field (Berensmeier 2006; Chen et al. 2013; Hejazian et al. 2015). Particle separation vastly depends on the intrinsic diamagnetic properties of the particles, which are not as sensitive as DEP-based particle separation based on the intrinsic dielectric properties of the particles (Pethig 2010b). Moreover, the fabrication of the microfluidic devices for effective magnetic field gradients is complicated. Particle separation methods using hydrodynamic force and mechanical filtration are mostly passive techniques and suitable for continuous operation. However, these size-based separation methods are not suitable for similar size particle separation. In addition, clogging and flow fluctuation can adversely affect particle separation in mechanical filtration (Di Carlo et al. 2007; Maruyama et al. 2009; Tauro et al. 2012). These methods also have limitations to apply various separation conditions because the size of the particle is the only parameter of the separate in general.

The acoustic-based particle separation uses ultrasonic transducer to generate acoustic radiation pressure as a driving

momentum to separate particles. The acoustic wave generated by ultrasonic transducer collects particles in the specific location inside the microfluidic platform (Ding et al. 2014; Lee et al. 2013a, 2015). The microchannel walls of microfluidic devices require good acoustic reflection for effective particle separation using the acoustic-based method. Thus, polymeric microfluidic device fabricated by soft lithography is not suitable to generate acoustic standing waves due to the poor acoustic reflection properties. Also, the acoustic separation is not effective for the particles of similar sizes with different membranes, structures and dielectric polarizabilities. In comparison to these methods, fabrication of microfluidic devices for DEP-based particle separation is easier and more cost effective. In addition, recent studies have shown that DEP-based particle separation techniques are suitable for efficient and high-throughput particle separation (Faraghat et al. 2017; Gupta et al. 2012; Hu et al. 2005).

Using microfluidic platforms, several DEP-based techniques have been employed over the last few decades. Based on the mode of operation, the dielectrophoretic platforms can be classified into two main groups: insulator-based DEP (iDEP) devices and electrode-based DEP (eDEP) devices (Saucedo-Espinosa et al. 2016). In general, insulating layers or arrays of insulating post/structures are employed between the electrodes to generate a spatially non-uniform electric field in iDEP-based devices (A. Braff et al. 2012; Gallo-Villanueva et al. 2014; Hawkins and Kirby 2010). In most cases, these insulating structures harm the strength of the generated non-uniform electric field and affect the strength of the DEP-force field (Benhal et al. 2020). Thus, to produce an adequate DEP-force field for a successful application, higher voltages are generally required in iDEP-based devices than eDEP-based devices (Saucedo-Espinosa et al. 2016), which may lead to rising temperatures inside the flow channel. This increase in temperature may trigger bubble formation and disrupt the flow of the particles, and thus significantly affects DEP-based particle separation (Cetin and Li 2008).

In recent times, eDEP devices have received more attention in microfluidic platforms as it is relatively easy to generate high electric field gradients (Benhal et al. 2020). With the advancement in micro- and nano-fabrication techniques, different types of electrode configurations and designs at the microscale were employed to develop DEP platforms. In contrast to iDEP-based devices, a significant portion of eDEP studies reported the use of low voltage and higher frequency electric fields (in the kilohertz to megahertz range) for micron and submicron particle separation. In general, the common trend of eDEP devices is to include an array of conductive electrodes (such as gold, copper, chromium). These metal electrodes are considered planar (2-D) as they are thin-film electrodes with a height range of a few hundred nanometers. The design of these thin-film electrodes

plays an important role in the generation of non-uniform electric fields. Based on the electrode arrangement, there are two options, namely horizontal and orthogonal electrode arrangements. In the horizontal arrangement, the electrodes are fabricated on one side of the flow channel (mostly on the bottom side) and fluid subsequently passes over them. These types of electrodes are usually referred to as interdigitated electrodes (IDE), and have been employed for different types of microparticle separation (Choi et al. 2018; Kwak et al. 2013; Park et al. 2016; Song and Bennett 2009; Wang et al. 2014). In contrast, in orthogonal electrode arrangements, the electrodes are placed opposite to each other in a parallel configuration (mostly on the top and bottom), with fluid flowing in between the electrodes (Kwak et al. 2021, 2019b, 2017; Mittal et al. 2007; Nejad et al. 2013; Thomas et al. 2019).

Generally, in both types of electrode configurations, the electric field gradient is stronger along the edges of the electrodes compared to the space between the electrodes. Conventionally, it is much easier to attract particles to the regions of stronger electric field gradients (p-DEP). But for biological particles (such as cells and viruses), it is desirable to use lower electric field strengths to minimize stress, transfection, and unwanted lysis of the bioparticles due to the applied electric field. Thus, for bioparticles, n-DEP based separation where particles can be pushed towards the regions of low electric field gradient is more desirable (Koklu et al. 2010; Punjiya et al. 2019; Thomas et al. 2019). For n-DEP based particle trapping, a uniform repelling/pushing force is required from the regions of the stronger electric field (Mauro 1980). It has been reported that an orthogonal type electrode configuration can generate pushing forces from the top, which alleviates particle trapping by n-DEP forces. For particles suspended in a flowing fluid, a repelling force from the top electrode in conjunction with the bottom electrode can effectively isolate particles (Tajik et al. 2020). Efforts have been made to fabricate three-dimensional (3-D) electrodes for particle separation and immobilization. The designs include a coiled electrode (Fathy and Lai 2020), DEP wells (Abdul Razak et al. 2013), extruded patterns (Iliescu et al. 2008), microwells (Mittal et al. 2007), a sidewall pattern (Wang et al. 2009) and top–bottom/face-to-face pattern electrodes (Kwak et al. 2021, 2019b, 2017; Punjiya et al. 2019; Yang et al. 1999). The 3-D microelectrodes were reported to produce effective DEP forces over a larger microfluidic device and can isolate and separate particles from a larger volume of fluid. Compared to planar electrodes, the 3-D electrodes interact more with the hydrodynamic drag forces on the suspended particles. In past research using IDE-based DEP devices, it was also reported that a closed-shape window (void space) in the planar electrode surface is capable to produce a weaker electric field gradient (Lombardini et al.

2010; Mahshid et al. 2018; Nakano et al. 2019; Nejad et al. 2013). Due to the stronger electric field along the edges of the electrodes, the closed-shaped windows can serve as the trapping locations of the particles inside the DEP device. By combining the advantage of closed-shape windows (which we refer to as corral traps) on the surface of an electrode with a counter electrode placed in an orthogonal configuration, an effective n-DEP force can be generated. The uniform pushing force from the top electrode can push particles downward, whereas the pushing force from the trap edges can push particles sideways towards the regions of the weaker electric field.

In this paper, we present a microfluidic platform with a 3-D electrode configuration for trapping microparticles using n-DEP. To harness the benefits of the orthogonal electrode configuration, we have utilized one electrode as the bottom plate and a counter electrode as the top plate of the microfluidic channel. We have employed three different basic geometric shapes, i.e. triangular, square, and circular, as corral traps in the bottom electrode, which, along with the counter electrode on top, create pushing forces from the sides and the top, respectively. In this study, a high frequency (1 MHz) AC electric field generated n-DEP forces that successfully trapped 4.42  $\mu\text{m}$  spherical carboxyl-functionalized polystyrene particles. The effects of spatial changes in the electric field gradient (linked to trap shape) were quantitatively studied by means of a 3-D trap stiffness analysis for single particles trapped inside the DEP traps. To date, there have been no studies to analyze trap shape effects on DEP trap stiffness. Trap stiffness is a measure of the restoring force acting on a particle inside the trap, which keeps the particle confined inside the trap, even under external perturbation (so long the perturbation is weaker than the trapping force). The equipartition theorem was employed to compute the trap stiffness of triangular, square, and circular corral traps by monitoring the thermal fluctuations of the trapped particles under the influence of an AC applied electric field at varying potentials (6  $V_{\text{p-p}}$  to 10  $V_{\text{p-p}}$ ) and a frequency of 1 MHz. The different corral trap shapes in the microfluidic device were also studied numerically to investigate the effect of geometry on n-DEP force generation.

## 2 Theory

Successful trapping of any particle using DEP depends on the electrical polarizability of that particle. When a particle suspended in a medium is exposed to an electric field, intrinsic charge separation inside the particle leads to an induced electric dipole moment. If the electric field is nonuniform, the electric field gradient will force the particle to move. This inducing motion is known as DEP, and the DEP force is given by

$$F_{DEP} = (p \cdot \nabla)E = (\alpha v E \cdot \nabla)E \quad (1)$$

where  $p$  is the induced dipole moment,  $\alpha$  is the polarizability factor,  $v$  is the volume of the particle, and  $E$  is the applied electric field. The differential operator  $\nabla$  indicates the gradient of the electric field. For a spherical particle with radius  $r$ , the polarizability factor  $\alpha$  can be described as (Pethig 2010a):

$$\alpha = 3\epsilon_0\epsilon_m Re[f_{CM}] \quad (2)$$

where  $\epsilon_0$  is the permittivity of free space ( $8.85 \times 10^{-12} F/m$ ),  $\epsilon_m$  is the relative permittivity of the suspending medium,  $Re$  indicates real part of a complex number, and  $f_{CM}$  is known as the Clausius–Mossotti (CM) factor.

The volume of a spherical particle is:

$$v = \frac{4}{3}\pi r^3 \quad (3)$$

The value of the CM factor ranges between -0.5 and 1.0 depending on the electrical properties (conductivity and permittivity) of the particle and the surrounding medium. For a spherical particle, the CM factor can be calculated as (Jones 1995):

$$f_{CM} = \frac{\epsilon_p^* - \epsilon_m^*}{\epsilon_p^* + 2\epsilon_m^*} \quad (4)$$

Where  $\epsilon_p^*$  and  $\epsilon_m^*$  are the complex permittivity of the particle and the suspension medium, respectively. For alternating current (AC) based DEP with an angular frequency  $\omega$ , the complex permittivity is defined as (Markx et al. 1996):

$$\epsilon^* = \epsilon - j\frac{\sigma}{\omega} \quad (5)$$

where  $\sigma$  is the electrical conductivity and  $j$  is the imaginary unit ( $\sqrt{-1}$ ). Combining Eqs. (1), (2) and (3) leads to the following expression for the DEP force:

$$F_{DEP} = 4\pi r^3 \epsilon_0 \epsilon_m Re[f_{CM}] (E \cdot \nabla)E \quad (6)$$

Equation (6) can be further simplified by the vector transformation of the electric field ( $E$ ):

$$F_{DEP} = 2\pi r^3 \epsilon_0 \epsilon_m Re[f_{CM}] \nabla E_{RMS}^2 \quad (7)$$

where  $E_{RMS}$  is the root mean square of the electric field and independent of the polarity of the potential applied to the electrodes. From Eq. (7), it can be seen that the DEP force is zero when the applied electric field is uniform ( $\nabla E_{RMS}^2 = 0$ ). With all other properties remaining constant, the DEP force will increase cubically with the size of the spherical particle. Referring to Eq. (4), it can be said that when the polarizability of the particle is higher than that of the surrounding

medium, the CM factor will be positive, which will favor p-DEP. In contrast, a negative value of the CM factor means the particle is less polarizable than the medium. According to Eqs. (4) and (5), it is evident that a change in frequency of the applied electric field (with other parameters remaining constant) will also change the value of the CM factor. Hence, under appropriate experimental conditions, a particle can be pulled towards or pushed away from regions with a strong electric field gradient by simply altering the frequency of the applied electric field. It is well established that for polymer-based microparticles suspended in weakly conducting solution (DI water), p-DEP occurs at lower frequencies and n-DEP occurs at higher frequencies (Lu et al. 2020; Weng et al. 2016). However, these ranges vary significantly based on electrode configuration, size, types, and polarization behavior of the particles as well as properties of the suspending medium.

Because electric fields are generated in a microfluidic channel filled with conducting medium (i.e. DI water), the effects of electroosmotic and electrothermal forces also need to be considered. The electrodes are exposed to the conducting medium and thus carry a net charge (from the dissociation of the chemical groups on the surface and adsorption of ions from the medium) and attract oppositely charged ions at the solid–liquid interface. At the same time, like-charged ions will be repelled from the surface. This thin layer of counter-ions and co-ions is known as the electric double layer (EDL) (Ramos et al. 1999). The applied nonuniform electric field with free charges in the EDL covering the surface of the electrodes perturb the balance of the EDL; the fluid motion induced by this interaction is known as electroosmotic flow (Dash and Mohanty 2014).

Depending on the operating conditions (i.e. frequency of the applied electric field, conductivity, and permittivity of the medium and the particle), electroosmotic flow can affect particle velocity and has the potential to influence DEP-based particle trapping. The induced motion of layers of the fluid body is governed by the Navier–Stokes equation and the continuity equation (Pribyl et al. 2008):

$$\rho_m \left( \frac{\partial v}{\partial t} + v \cdot \nabla v \right) - \eta_m \nabla^2 v = -\nabla p + f_{BodyForce} \quad (8)$$

$$\nabla \cdot v = 0 \quad (9)$$

where  $\rho_m$  and  $\eta_m$  are the density and kinematic viscosity of the suspending medium,  $v$  is the flow velocity, and  $\nabla p$  is the pressure gradient. The body force per unit volume ( $f_{BodyForce}$ ) is induced by the electric field, which depends on the electric charge density ( $\rho_E$ ) and the electric field ( $E$ ). The Laplacian term implies the diffusion of momentum (governed by viscosity) and can be interpreted as velocity difference at a point and the mean velocity of the surrounding fluid volume. Equation (9)



implies that divergence of the velocity field is zero everywhere. It was reported in past studies that the effect of electroosmotic force induced by high frequency (i.e. 1–100 MHz) electric field has no significant effect on particle trapping in microfluidic platforms (Park and Beskok 2008; Ramos et al. 1999).

Joule heating can generate another form of electrohydrodynamic force, namely electrothermal flow. Joule heating causes a rise in temperature inside the microfluidic device due to the resistivity of the conductors when electric current pass through it. The hydrodynamic force generated by the electrothermal flow can also be formulated using the Navier–Stokes equation. A simplified theoretical model implies that Joule heating is proportional to the conductivity of the medium and square of the applied electric field, i.e.  $\sigma_m E^2$  (Sin et al. 2010). Hence, with the same electric field applied, the effect of electrothermal flow linearly increases with the change in conductivity of the suspending medium. Past studies have revealed that the effect of electrothermal flow in a higher frequency ( $\geq 1\text{MHz}$ ) electric field and low conductivity medium has an insignificant effect on microfluidic particle manipulation. Moreover, flow patterns induced by electrothermal flow inside the microfluidic device with two oppositely charged electrodes at orthogonal configuration produce counter-rotating vortices near the electrodes. These vortices will not produce any net flow, and the vortices will not affect particles trapped by n-DEP (Koklu et al. 2010). It was also reported in a recent study that localized heating was from the dielectric loss rather than joule heating in interdigitated electrodes (Kwak et al. 2019a). The electrodes were electrically insulated with a dielectric material and were tested with media with different conductivities (i.e. DI water, sodium chloride solution, and phosphate-buffered saline).

A particle suspended in a medium is also subjected to the hydrodynamic drag force. Usually, fluid flow inside the microfluidic channels is in the creeping flow regime (Reynolds number  $< 0.5$ ) because of the small dimensions and low flow rate. The associated drag force can be estimated from the modified Stokes equation which accounts for particle–wall interaction from shear layers:

$$F_{Drag} = -6\pi r \eta_m h S K \quad (10)$$

Here,  $r$  is the particle radius,  $\eta_m$  is the viscosity of the medium,  $h$  is the height of the particle within the shear field,  $S$  is the shear rate, and  $K$  is a coefficient that incorporates wall effects, taken to be 1.7005 (Thomas et al. 2009). The shear rate  $S$  can be computed from the flow velocity and cross-section of the flow channel (Punjiya et al. 2019):

$$S = \frac{8v}{d_h} \quad (11)$$

where  $v$  is the flow rate and  $d_h$  is the hydraulic diameter. As the cross-section of the microchannel is rectangular, the hydraulic diameter  $d_h$  is equivalent to

$$d_h = \frac{2w_c h_c}{w_c + h_c} \quad (12)$$

where  $w_c$  is the width of the channel and  $h_c$  is the height of the channel, which are 12.7 mm and 30  $\mu\text{m}$ , respectively.

## 3 Materials and methods

### 3.1 Particles and suspending medium

Carboxyl-functionalized polystyrene spherical particles with a mean diameter of 4.42  $\mu\text{m}$  (Spherotech, USA) were used throughout the experiment. The carboxyl-functionalized polystyrene particles are widely used in various studies as a model particle (Abd Rahman et al. 2017; Chen and Yuan 2019; Saucedo-Espinosa et al. 2016; Song et al. 2012), because of their stable negative surface charge (Dorney 2013). The surface of the traps used in this study is bare glass surface which acquires negative charge when in contact with the medium and fluid (Behrens and Grier 2001). The negative surface charges of the trap surface and the carboxyl-functionalized polystyrene particles reduce the potential adhesion of the particles on the trap surface due to repulsion between the negatively charged surfaces. The stock solution of the particles was washed three times with Milli-Q deionized (DI) water by centrifugation and resuspension. DI water was used to dilute the stock solution of 5% (w/v) to 0.0001% (w/v). The conductivity was measured to be 2  $\mu\text{S cm}^{-1}$  (at 25  $^\circ\text{C}$ ) using a conductivity meter (Horiba LAQUAtwin EC-11). Freshly prepared microparticle suspensions were gently vortexed to disrupt aggregations of the particles before all the experiments.

### 3.2 Device preparation and equipment

The microfluidic DEP device was fabricated using a 1-inch by 1-inch microscope slide (thickness = 1 mm) as a substrate. Three basic geometric shapes, namely triangular, square, and circular trap patterns were first patterned using the standard photolithography technique. The fabrication steps of the microfluidic DEP device are shown in Fig. S1 in the Supplementary Information.

In brief, the slide was first washed ultrasonically with acetone (5 min) and then in piranha solution (30 min) to clean off organic materials. The surface was then coated with hexamethyldisilane (HMDS) vapor in a vacuum chamber to convert the clean hydrophilic surface to a hydrophobic surface. This ensured better adhesion of the photoresist layer used in the next step. A  $\sim 1\ \mu\text{m}$  thick layer of AZ 5214E-IR photoresist

(Micro Chemicals, USA) was coated on the HMDS treated glass surface using an SCS 6800 spin coater (SCS, USA). After that, the trap patterns (triangular, square, and circular) were formed through UV exposure (PLA-501-FA, Canon, Japan) and subsequent development of the substrate using AZ 400 K Developer (AZ Electronic Materials, USA). A 100 nm thick chromium layer was deposited using the physical vapor deposition process (KV-301, Key High Vacuum Products, Inc., USA), and then patterned by a lift-off process using acetone under ultra-sonication. Chromium was selected as the thin film electrodes and fabricated through thermal evaporation. The main reason to select chromium is its sublimation properties and high vapor pressure (100 mT at 1500 °C) compared to gold (30 mT at 1500 °C) and platinum (1  $\mu$ T at 1500 °C) (Sarangan 2016). This enables chromium to be thermally deposited on the substrate faster with less energy usage. Moreover, chromium is less expensive than the noble metals, i.e., gold and platinum, typically used in thin film-based metal electrodes. As shown in Fig. 1a, an orthogonal electrode configuration was created with a transparent indium-tin-oxide (ITO) coated 1-inch by 1-inch glass slide (Nanocs Inc, USA) as the counter electrode. The thickness and surface resistivity of this ITO coated glass was 1.1 mm and 10  $\Omega$ /square, respectively. A closed microfluidic channel was created by placing 30  $\mu$ m thick polyethylene terephthalate (PET) double sided-adhesive spacers (Nitto Denko Co, Japan) between the chromium electrode (bottom) and ITO counter-electrode (top). Adhesive copper foil tape (JVCC CFL-5CA, electrical resistance: 0.003 Ohms/square inch) was used to attach the wires to the electrodes. Inlet

and outlet tubing were attached to a pair of holes created on the ITO-coated glass with a highspeed mini-drill. A KDS 200 syringe pump (KD scientific, USA) was used to inject the fluid containing the microparticles into the device. The square trap had a side length of 30  $\mu$ m and an area of 900  $\mu$ m<sup>2</sup>; the triangular trap had the same area as the square trap with a base of 30  $\mu$ m, height of 60  $\mu$ m, and a vertex angle of 28.07°. For the circular trap, however, the diameter was kept as 30  $\mu$ m, which resulted in a trap area of 706.86  $\mu$ m<sup>2</sup>. Figure 1a presents a schematic illustration of the microfluidic DEP device and experimental setup.

An Agilent 33250A arbitrary waveform generator was used to apply sinusoidal AC electric potentials of up to 10  $V_{p-p}$  at 1 MHz. An optical upright microscope (BX53F, Olympus, Japan) fitted with a high-speed camera (Bonito CL-400, Allied Vision Technologies, USA) was used for real-time image observation and recording. All images were acquired at 50 frames/sec for 40 s with a resolution of 2320  $\times$  1725 pixels. For particle movements and analysis, the Particle Tracker plugin (Mosaic Toolbox Suite) in ImageJ software (V1.52P) was used. Before any experiment, the fabricated microfluidic DEP device was washed with DI water three times and dried at room temperature. Experiments started with filling up the device with the suspending medium containing 4.42  $\mu$ m polystyrene particles. An AC electric potential was applied to the electrodes after a wait time of 5 min to avoid movements and internal flow of the particles. Figure 1b shows the fabricated microfluidic DEP device with triangular, square, and circular traps with 4.42  $\mu$ m particles trapped in each of them. Videos and still

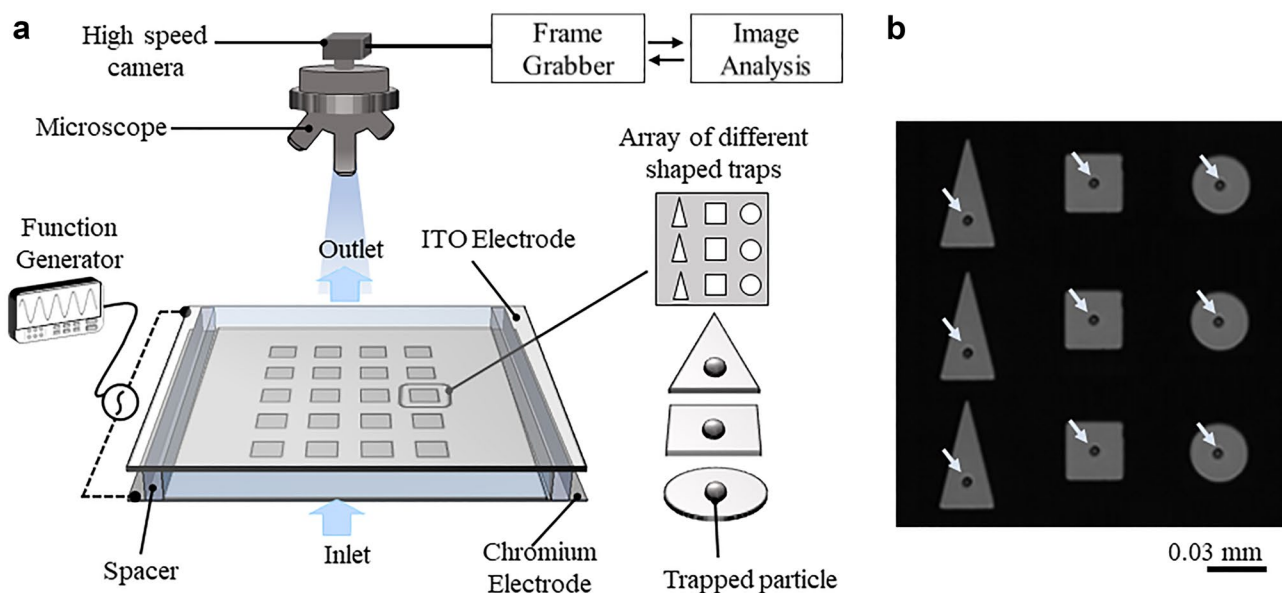


**Fig. 1** Schematic illustration and picture of the microfluidic device used in the experiments. **a** Schematic drawing of the setup with the device containing triangular, square, and circular traps, **b** The fabri-

cated device containing triangular, square, and circular traps with trapped particles (marked)

images of the un-trapped and trapped particles were taken to analyze particle behavior under the effect of the electric field with potentials from  $6 V_{P,P}$  to  $10 V_{P,P}$  at 1 MHz. To calculate the trap stiffness, the series of images captured by the high-speed camera was first converted to 8-bit gray scale images. The Sobel edge detector was then applied to all the images to highlight sharp changes in intensity in the active image. This enables the detection of the boundary of all spherical particles in the images. In the next step, the ParticleTracker plugin was used to determine the locations of the particles, which were then linked with all the subsequent images. These location data were then extracted and used for the computation of trap stiffness.

## 4 Results and discussion

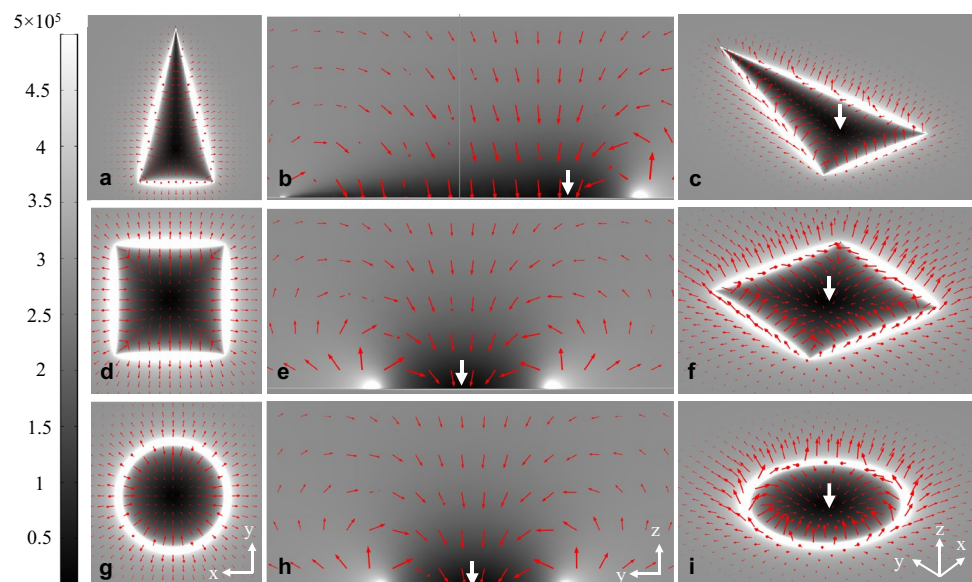
### 4.1 Numerical simulation of the effect of geometry

A finite element analysis was performed with COMSOL Multiphysics software (V5.2) using the creeping flow, electrostatics, and particle tracing module in a coupled 3-D model (Lee et al. 2017; Rahman et al. 2021). A Dirichlet boundary condition with an applied voltage equivalent to the  $V_{RMS}$  value of the electric potential of  $6 V_{P,P}$ ,  $7 V_{P,P}$ ,  $8 V_{P,P}$ ,  $9 V_{P,P}$ , and  $10 V_{P,P}$ , with opposite polarity, was imposed at the top and bottom electrodes. The other boundaries were set to be perfectly insulated. Infinite inlets and outlets were assumed at the two ends of the channel and periodic boundary conditions were applied at the opposite sides. Figure S2 in the Supplementary Information shows the computation domain used in this study. The model was first solved for

the creeping flow module as the stationary study. In the next step, the model was analyzed in the frequency domain to study the effect of the applied electric field ( $6 V_{P,P}$  to  $10 V_{P,P}$ ) at 1 MHz. As the model was solved for a no-flow condition, the effect of hydrodynamic drag forces were found to be insignificant. The CM factor was computed with relevant parameters in MATLAB and subsequently used to compute the DEP force. The electric field gradient data were used in the equations discussed above to calculate the overall DEP force.

Figure 2 shows the magnitude and direction of the DEP force field acting on  $4.42 \mu\text{m}$  particles in triangular, square, and circular traps inside the microfluidic DEP device. Here, the directions and relative magnitudes of the DEP forces acting on a particle are portrayed by the arrows, whereas the grayscale indicates the magnitude of the electric field. As shown in Fig. 2, the electric field strength varied greatly across the traps, with a zero value in the geometric centroid (black color) and maximum at the edges of the traps (white color). In the case of n-DEP based particle trapping, a particle will be pushed away from the edges of the traps towards the low strength electric field gradient. The trapping location (in the xy-plane) will be dictated by the balance of the inward pushing forces from the edges of the trap. The white arrows inside the triangular, square, and circular traps indicate the predicted particle trapping locations based on the finite element simulation. The cross-sectional views of the triangular, square, and circular traps (Fig. 2b, e, and h, respectively) indicate that a particle will be pushed from the sides and from the top towards the trapping location. At the same time, a particle can be pushed away from the trap due to the outward pushing force along the trap edge.

**Fig. 2** Magnitude and direction of the computed DEP force acting on a single  $4.42 \mu\text{m}$  polystyrene particle with an applied electric field of  $10 V_{P,P}$  at 1 MHz, calculated from finite element simulation using COMSOL Multiphysics. The arrows indicate normalized DEP forces with the electric field magnitude (V/m) in grayscale. The top, cross-section, and isometric view for a triangular (a-c), square (d-f) and circular (g-i) trap shows the predicted particle trapping location (white arrows) using n-DEP, i.e. the weakest electric field region



Here, the traps act as a 3-D closed cage when DEP is ON (i.e. an electric field is applied), in which case the particles will be pushed down towards the centroid region of the traps. The simulation also shows that the DEP force will keep a particle trapped and the DEP force will increase with the increase of applied electric potential.

In this study, we have not considered the flow of the medium (i.e. flow-through mode) and the analysis was conducted for a no-flow condition. Hence, the initial locations of dispersed particles were important in the experiments conducted for particle trapping. In contrast, in flow through mode, the induced drag force can overcome the repelling force from the boundary of the traps. For any particle in the favorable trapping locations, the inward force will push the particle towards the bottom of the trap, where the electric field strength is at a minimum. It was found that the trapping location (in the  $xy$ -plane) for the three different geometric shapes was, in each case, the geometric centroid.

Two different 3-D uncoupled models were also computed numerically to study the effect of the electroosmotic flow and electrothermal flow using the creeping flow, electrostatics, and heat transfer in fluids modules in COMSOL Multiphysics. The flow velocities at the trapping location for each of the geometries were extracted to compute the effect of drag on particle trapping by DEP. It was found that for the operating conditions and the materials used in this study, the effect of the drag force at the particle trapping location is insignificant. The overall DEP force acting on a  $4.42\ \mu\text{m}$  spherical particle at the trapping location for the triangular, square, and circular traps is depicted in Fig. 3. The overall DEP force is the resultant of the DEP force acting in  $x$ -,  $y$ - and  $z$ -axis at the trapping location, the centroid of each of the different shape traps. The DEP force was computed at  $2.21\ \mu\text{m}$  height from the bottom of the electrode surface as the diameter of the particle was  $4.42\ \mu\text{m}$ . As shown, the DEP force increases gradually with an increase in potential from  $6\ V_{p,p}$  to  $10\ V_{p,p}$  at  $1\ \text{MHz}$ . The non-linear dependence of DEP force on applied potential is expected given that the DEP force is proportional to the square of the electric field gradient ( $\nabla E^2$ ), which is a non-linear function. In the numerical computation, the estimated DEP force was increased up to 2.7 times when changing the applied potential from  $6\ V_{p,p}$  to  $10\ V_{p,p}$  at  $1\ \text{MHz}$  for all three trap shapes. It is also evident from the finite element simulation that amongst the three different shapes, the triangular trap produces the strongest DEP force at the trapping location, whereas the square trap produced the weakest DEP force. At the maximum electric potential ( $10\ V_{p,p}$ ), the DEP force at the triangular trap was found to be about 17% higher than the DEP force at the circular trap, and the latter was estimated to be 18% higher compared to the square trap.

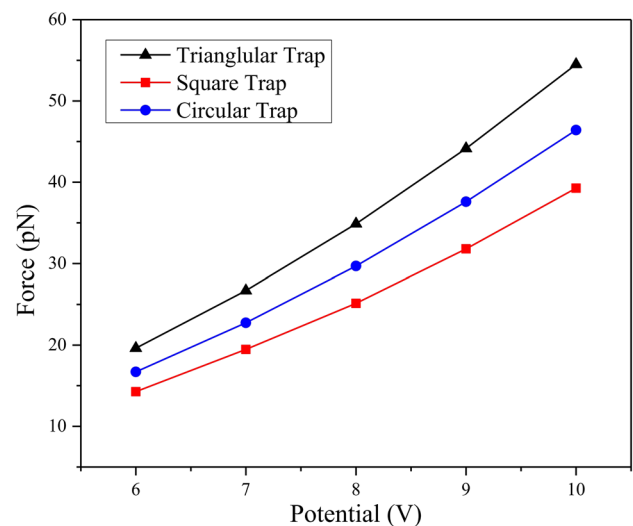


**Fig. 3** Effect of applied potential ( $6\ V_{p,p}$  to  $10\ V_{p,p}$  at  $1\ \text{MHz}$ ) on the DEP force acting on a  $4.42\ \mu\text{m}$  polystyrene spherical bead in triangular, square and circular traps from finite element simulations using COMSOL Multiphysics software

#### 4.2 Effect of geometric shapes on DEP force and trap stiffness

A large set of experiments was performed to observe trapping behavior of  $4.42\ \mu\text{m}$  particles with electric potentials from  $6\ V_{p,p}$  to  $10\ V_{p,p}$  at  $1\ \text{MHz}$  applied to the microfluidic DEP device containing triangular, square, and circular traps. As displayed in Fig. 1b, particles were trapped in triangular, square, and circular traps using the developed microfluidic DEP device; the trapping of particles was also confirmed in the finite element simulation with the particle tracing module. High-speed images from the experiments were analyzed to compare the trapping characteristics for the different trap shapes. It was observed that the trapped particles were not trapped in a stationary fashion, but that they were fluctuating continuously with very small displacements within the trapping zone. As a baseline for the fluctuations of trapped particles, the movements of particles without an applied electric field (i.e. with no DEP force acting on them) were also recorded. For this, an arbitrary particle was randomly selected from the dispersed particles inside the microfluidic device before applying the electric field. The movement of an un-trapped particle in the  $xy$ -plane was reconstructed from the frames of the high-speed video and converted to  $\mu\text{m}$  displacements. The trajectory displayed in Fig. 4 indicates pure Brownian motion due to continuous collisions with molecules of the surrounding medium (Almendarez-Rangel et al. 2018; Cohen and Moerner 2006; Guan et al. 2011; Volpe et al. 2007).

In the next step, the movements of single particles trapped in each of the triangular, square, and circular traps were



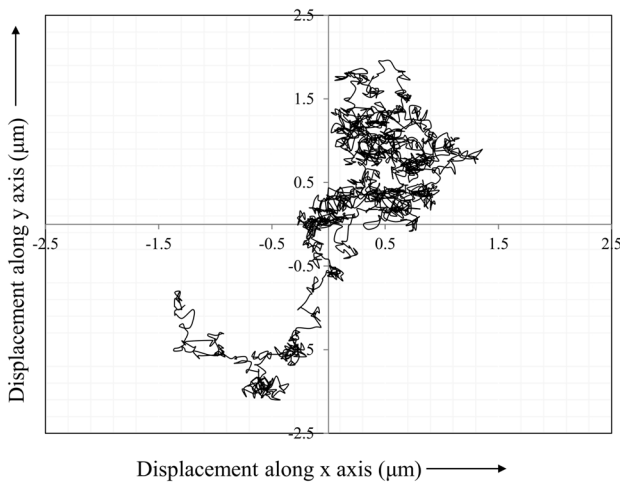


**Fig. 4** Trajectory of a 4.42  $\mu\text{m}$  particle without DEP (no electrical field applied) showing pure random movements (Brownian motion) under no-flow conditions

analyzed under the steady-state conditions. Particle locations relative to the trapping location (geometric centroid) of the trap were measured in pixels and converted to  $\mu\text{m}$  for each frame. The experiments were repeated three times with DEP forces generated by applying 6  $V_{\text{P-P}}$ , 7  $V_{\text{P-P}}$ , 8  $V_{\text{P-P}}$ , 9  $V_{\text{P-P}}$ , and 10  $V_{\text{P-P}}$  at 1 MHz to triangular, square, and circular traps. As shown in Fig. 5, the xy-trajectories of a single trapped particle (under DEP force) exhibited a much more restricted movement compared to an un-trapped particle (without DEP force) when plotted at the same scale.

The stronger confinement of the trapped particle when the applied electric potential is increased also indicates a rise in the DEP force from the edges of the traps, which support the findings from the finite element simulations. Figure 5 clearly demonstrates trapping of particles by n-DEP; the trapping locations arise from the balance of DEP forces originating at the edges of the traps and were found to be the same as those predicted by the finite element simulation. The strong n-DEP behavior was observed for all three different trap shapes under the applied AC voltage. A comparison of the particle trajectories at 6  $V_{\text{P-P}}$  vs. 10  $V_{\text{P-P}}$  shows that the lateral movement of trapped particles is restricted to a very small trapping region.

The restricted movement of the trapped particle shown in Fig. 5 a-e exhibits less movement in the lateral direction and more movement in the longitudinal direction. This behavior is supported by the shape of the triangular trap, which has a base of 30  $\mu\text{m}$  and a height of 60  $\mu\text{m}$ . Similarly, the forces from the sides of the square trap restrict the motion of a trapped particle (Fig. 5f-j). In the case of the circular trap, the DEP forces generated in the radial direction confine the particle to the central area (Fig. 5k-o), which is the low-field region according to the finite element simulations.

Along with the locations in the xy-plane, the locations of the trapped particles along the z-axis (height) were also analyzed for all three trap shapes under the operating conditions discussed in Fig. 5. We have utilized the general defocusing particle tracking (GDPT) tool, a particle tracking tool developed in MATLAB by Barnkob et al. (Barnkob et al. 2015; Barnkob and Rossi 2020). This particle-tracking technique

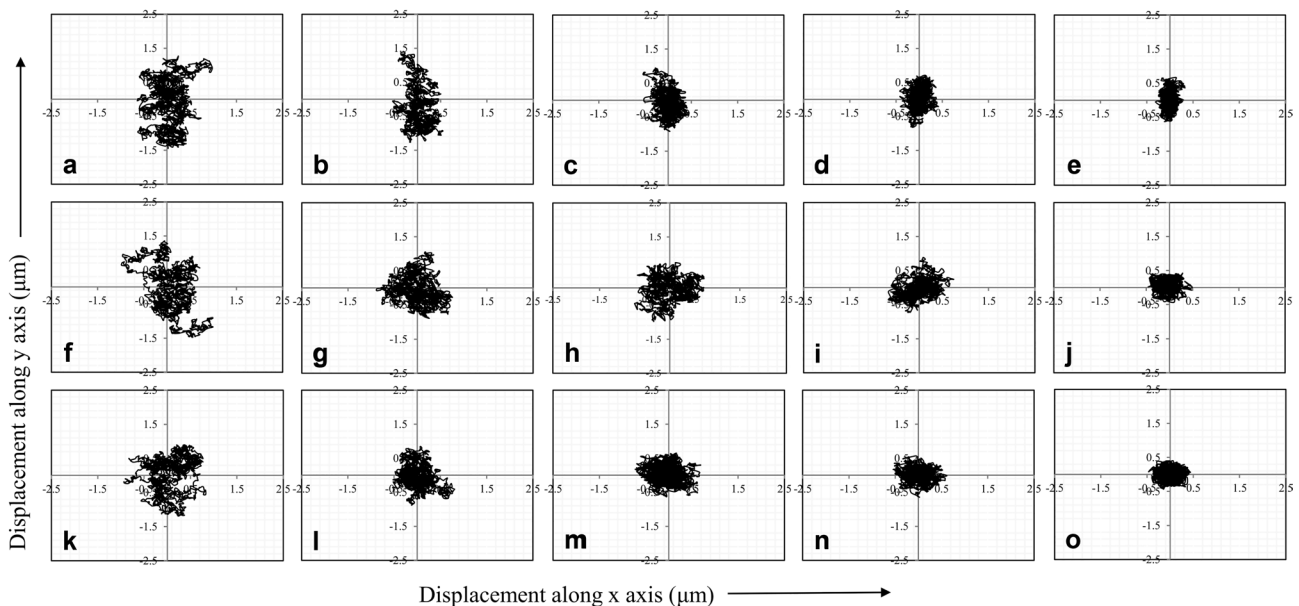


**Fig. 5** Trajectories in the xy-plane of 4.42  $\mu\text{m}$  particles trapped by n-DEP, generated by applying electric potentials of 6, 7, 8, 9 and 10  $V_{\text{P-P}}$  (from left to right) at 1 MHz to triangular (a-e), square (f-j) and circular (k-o) traps, respectively

obtains the particle's height information based on the defocusing patterns from a series of particle images in a specific range of  $z$  coordinates.

As depicted in Fig. 6, for applied electric potentials of  $6 V_{p,p}$ ,  $8 V_{p,p}$ , and  $10 V_{p,p}$  at 1 MHz, the vertical movement (along the  $z$ -axis) of trapped particles was confined to  $\sim 2 \mu\text{m}$ . The height locations for trapped particles in triangular, square, and circular traps for applied electric potentials of  $6 V_{p,p}$  to  $10 V_{p,p}$  at 1 MHz is included in the Supplementary Information (Figure S3). The similar vertical movements of the trapped particles in triangular, square, and circular traps signify that the orthogonal electrode configuration plays an important role for vertical confinement. The downward force exerted by the counter-electrode is the key reason for the restricted movement of trapped particles

along the  $z$ -axis, while the trap shape is the decisive factor for particle confinement in the  $xy$ -plane.

For the quantitative analysis of the motions of trapped particles, we have employed the equipartition theorem, which relates the energy of thermal fluctuations with the positional variances from the steady-state condition. For an absolute temperature  $T$  and trap stiffness  $k_{trap}$ , the equipartition theorem states (Guan et al. 2011):

$$k_{trap} = k_B T (\sigma^2)^{-1} \quad (13)$$

where  $k_B$  is the Boltzmann constant and  $\sigma^2$  is the positional variance of a trapped particle from the trap center. The statistical positional variance data were extracted from the trajectories of trapped particles using the particle tracking

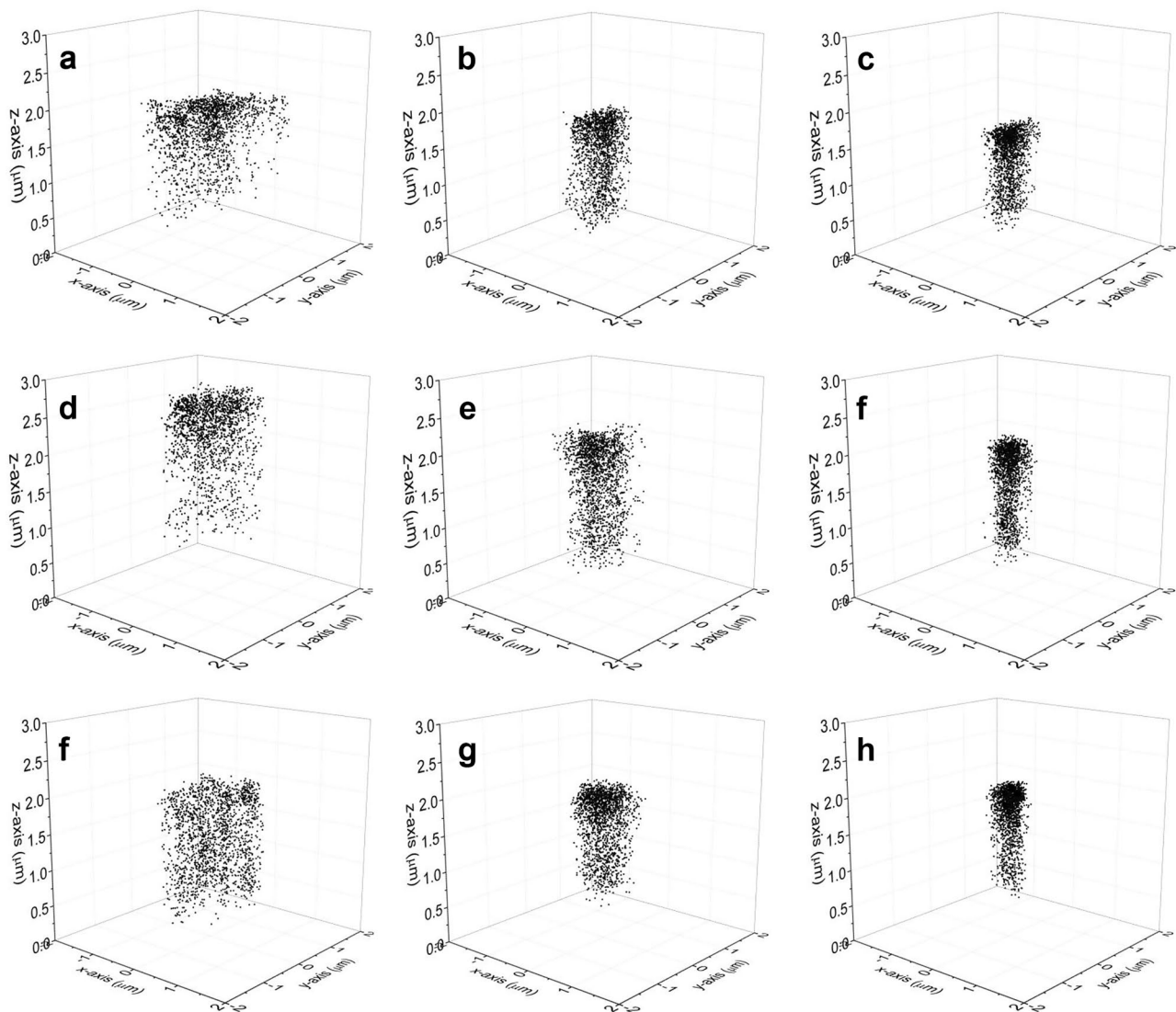


**Fig. 6** Three-dimensional (3-D) movements (along the  $x$ -,  $y$ - and  $z$ -axis) of trapped  $4.42 \mu\text{m}$  polystyrene particles in a triangular trap (a-c), square trap (d-f), and circular trap (f-h) at  $6 V_{p,p}$ ,  $8 V_{p,p}$ , and  $10 V_{p,p}$  at 1 MHz

package in the ImageJ software. This process was repeated to obtain three different data sets similar to Fig. 5 for the triangular, square, and circular shape traps.

The overall trap stiffness for the three trap shapes is shown in Fig. 7, and the trends found were very similar to the computed DEP forces in the finite element simulation. The overall trap stiffness of the triangular trap was found to be the strongest, and the trap stiffness of the square trap was the weakest. The non-linear behavior of trap stiffness in response to the applied electric potential is again expected given the non-linear dependence of the DEP force on the electric field gradient (Eq. 7). The developed device has the potential to trap multiple particles within the same trap, but the trap stiffness was computed for single particles only to avoid the effect of particle–particle interaction under the influence of the applied electric field. The overall trap stiffness increased more than eight-fold in the triangular trap when the potential was ramped up from 6  $V_{p-p}$  to 10  $V_{p-p}$ , while it increased by more than six times for square and circular traps over the same range of applied potential. As the experiments were conducted under no-flow conditions, the effects of flow and associated drag force were not included in the computation of the trap stiffness.

Interestingly, at the maximum electric potential (10  $V_{p-p}$ ), the overall trap stiffness of the triangular trap was found to be about 26% higher than the trap stiffness of the circular trap. Under similar conditions, the square trap was about 60% weaker than the triangular trap and 27% weaker than the circular trap.

Past studies confirmed that the thermal changes generated from the applied AC potential in microchannels is well matched with the predicted values obtained by the finite

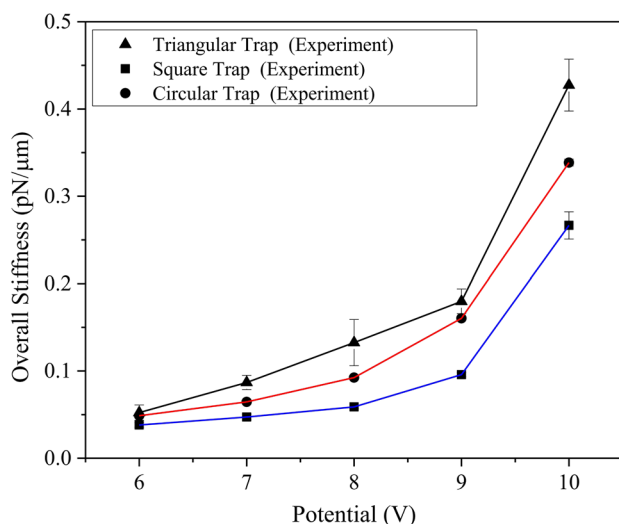


**Fig. 7** Effect of applied potential (6  $V_{p-p}$  to 10  $V_{p-p}$ ) on trap stiffness based on trapped 4.42  $\mu\text{m}$  polystyrene beads in triangular, square, and circular traps at 1 MHz

element analysis for the range of potentials and frequencies used in this study (Cetin and Li 2008; Gallo-Villanueva et al. 2014; Kwak et al. 2019a; Yan et al. 2017). From the finite element simulation, it was found that the temperature will increase by 0.4 and 1.6  $^{\circ}\text{C}$  over 40 s when 6 and 10  $V_{p-p}$  at 1 MHz of AC is applied. Total run time for image acquisition in this research was 40 s for stiffness analysis. Thus, the maximum temperature increased during the stiffness measurement was 1.6  $^{\circ}\text{C}$ .

The stronger Brownian motion of the trapped particles is expected due to the increased temperature and thermal fluctuations. The effect of thermal fluctuation would be higher with higher potential, because the thermal fluctuation is proportionally increased with applied potential. Thus, the actual stiffness with higher potential supposed to be higher than calculated stiffness, because the thermal fluctuation was included in the stiffness calculation. However, the effect of heat generation on trap stiffness among different trap geometries was not separately considered in this study, because the thermal effect is supposed to be the same for tested traps, as long as applied potential, AC frequency, and trap area are consistent. In depth analysis on the effect of thermal fluctuation on trap stiffness is under investigation now. The developed devices have been used to trap specific-sized, spherical protein particles from a mixture of different size proteins particles (Kwak et al. 2021). Trapping of other biological particles (cells and viruses) are under investigation using the developed 3-D microfluidic DEP device.

## 5 Conclusion

In this work, we designed a 3-D microfluidic DEP device containing triangular, square, and circular traps. The device employs n-DEP forces to capture particles at a specific location inside the traps. The objective of this research was to quantitatively study the effect of different geometric shapes on particle trapping with traps of similar dimensions. It was assumed that the circular trap would be strongest due to having the smallest area amongst the three different trap shapes. But interestingly, from both numerical and experimental studies, it turned out that the triangular trap generated the strongest n-DEP forces at 6  $V_{p-p}$ , 7  $V_{p-p}$ , 8  $V_{p-p}$ , 9  $V_{p-p}$ , and 10  $V_{p-p}$  and 1 MHz. When comparing triangular and square traps of the same area, triangular traps were found to be about 60% stronger (in terms of trap stiffness) than square traps at 10  $V_{p-p}$  and 1 MHz, while the circular traps were found to be 27% stronger than square traps under these conditions. All three different trap shapes generated the strongest DEP forces at the highest applied potential (10  $V_{p-p}$  at 1 MHz). The different shape traps were arranged in the array with significant inter-spacing between the traps to avoid any interference from the adjacent traps. The traps

can be arranged more densely with different orientations to improve trapping efficiency. The effect of spacing between traps and orientation is under investigation now.

In this study, trap stiffness was not evaluated with an inflow condition as the flow-induced drag force would become a dominant force under these circumstances. Moreover, only the trap stiffness for single trapped particles was evaluated to avoid the complicating effects of particle–particle interactions and associated dynamics inside the traps. The operating conditions of this microfluidic trapping device are easily controllable, and the corral trap arrays can be fabricated for parallel operation. The research can be extended to explore ways to further improve the trapping force, increase the efficiency under different operating conditions, and investigate other corral trap shapes. Although we have characterized the trapping force and trap stiffness using polystyrene spherical beads as surrogate particles, the developed device has the potential to be used with biological particles, for example cell patterning or cell isolation.

**Supplementary Information** The online version contains supplementary material available at <https://doi.org/10.1007/s10544-021-00570-3>.

**Funding** No funding was received to assist with the preparation of this manuscript.

**Data availability** The datasets generated during and/or analyzed during the current study are available from the corresponding author on reasonable request.

**Code availability** The code developed and used during the current study are available from the corresponding author on reasonable request.

## Declarations

**Competing interests** The authors have no conflicts of interest to declare that are relevant to the content of this article.

## References

- N. Abd Rahman, F. Ibrahim, and B. Yafouz, *Sensors* **17**, 449 (2017).  
M. A. Abdul Razak, K. F. Hoettges, H. O. Fatoyinbo, F. H. Labeed, and M. P. Hughes, *Biomicrofluidics* **7**, (2013).  
W.A. Braff, A. Pignier, C.R. Buie, *Lab. Chip* **12**, 1327 (2012)  
E. O. Adekanmbi and S. K. Srivastava, *Bio-Inspired Technol.* (2019).  
G. Aragay, J. Pons, A. Merkoci, *Chem Rev* **111**, 3433 (2011)  
A. Ashkin, J.M. Dziedzic, T. Yamane, *Nature* **330**, 769 (1987)  
R. Barnkob, C.J. Kähler, M. Rossi, *Lab. Chip* **15**, 3556 (2015)  
R. Barnkob, M. Rossi, *Exp. Fluids* **61**, 110 (2020)  
F.F. Becker, X.B. Wang, Y. Huang, R. Pethig, J. Vykoukal, P.R. Gascoyne, *Proc. Natl. Acad. Sci.* **92**, 860 (1995)  
S.H. Behrens, D.G. Grier, *J. Chem. Phys.* **115**, 6716 (2001)  
P. Benhal, D. Quashie, Y. Kim, J. Ali, *Sensors* **20**, 5095 (2020)  
S. Berensmeier, *Appl. Microbiol. Biotechnol.* **73**, 495 (2006)  
A. Castellanos, A. Ramos, A. González, N.G. Green, H. Morgan, *J. Phys. Appl. Phys.* **36**, 2584 (2003)  
B. Cetin, D. Li, *Electrophoresis* **29**, 994 (2008)  
K.L. Chan, P.R. Gascoyne, F.F. Becker, R. Pethig, *Biochim. Biophys. Acta BBA-Lipids Lipid Metab.* **1349**, 182 (1997)  
A. Chen, T. Byvank, W.-J. Chang, A. Bharde, G. Vieira, B.L. Miller, J.J. Chalmers, R. Bashir, R. Sooryakumar, *Lab. Chip* **13**, 1172 (2013)  
C. Chen, J. Skog, C.-H. Hsu, R.T. Lessard, L. Balaj, T. Wurdinger, B.S. Carter, X.O. Breakefield, M. Toner, D. Irimia, *Lab Chip* **10**, 505 (2010)  
Q. Chen, Y.J. Yuan, *RSC Adv.* **9**, 4963 (2019)  
S. Choi, K. Ko, J. Lim, S. H. Kim, S.-H. Woo, Y. S. Kim, J. Key, S. Y. Lee, I. S. Park, and S. W. Lee, *Sensors* **18**, (2018).  
A.E. Cohen, W. Moerner, *Proc. Natl. Acad. Sci. U. S. A.* **103**, 4362 (2006)  
L. D'Amico, N.J. Ajami, J.A. Adachi, P.R.C. Gascoyne, J.F. Petrosino, *Lab. Chip* **17**, 1340 (2017)  
S. Dash, S. Mohanty, *Electrophoresis* **35**, 2656 (2014)  
R.T. Davies, J. Kim, S.C. Jang, E.-J. Choi, Y.S. Gho, J. Park, *Lab. Chip* **12**, 5202 (2012)  
D. Di Carlo, D. Irimia, R.G. Tompkins, M. Toner, *Proc. Natl. Acad. Sci.* **104**, 18892 (2007)  
X. Ding, Z. Peng, S.-C.S. Lin, M. Geri, S. Li, P. Li, Y. Chen, M. Dao, S. Suresh, T.J. Huang, *Proc. Natl. Acad. Sci.* **111**, 12992 (2014)  
P.S. Dittrich, A. Manz, *Nat. Rev. Drug Discov.* **5**, 210 (2006)  
J. Dorney, *Doctoral* (2013).  
S.A. Faraghat, K.F. Hoettges, M.K. Steinbach, D.R. van der Veen, W.J. Brackenburg, E.A. Henslee, F.H. Labeed, M.P. Hughes, *Proc. Natl. Acad. Sci.* **114**, 4591 (2017)  
J. Fathy and Y. Lai, *J. Micromechanics Microengineering* **30**, 035009 (2020).  
R.C. Gallo-Villanueva, M.B. Sano, B.H. Lapizco-Encinas, R.V. Dávalos, *Electrophoresis* **35**, 352 (2014)  
S.A. Glazier, M.A. Arnold, *Anal. Chem.* **63**, 754 (1991)  
W. Guan, S. Joseph, J.H. Park, P.S. Krstić, M.A. Reed, *Proc. Natl. Acad. Sci.* **108**, 9326 (2011)  
V. Gupta, I. Jafferji, M. Garza, V. O. Melnikova, D. K. Hasegawa, R. Pethig, and D. W. Davis, *Biomicrofluidics* **6**, (2012).  
P.M. Hansen, V.K. Bhatia, N. Harrit, L. Oddershede, *Nano Lett.* **5**, 1937 (2005)  
B.G. Hawkins, B.J. Kirby, *Electrophoresis* **31**, 3622 (2010)  
M. Hejazian, W. Li, N.-T. Nguyen, *Lab. Chip* **15**, 959 (2015)  
K.F. Hoettges, Y. Hübner, L.M. Broche, S.L. Ogin, G.E.N. Kass, M.P. Hughes, *Anal. Chem.* **80**, 2063 (2008)  
X. Hu, P.H. Bessette, J. Qian, C.D. Meinhardt, P.S. Daugherty, H.T. Soh, *Proc. Natl. Acad. Sci. U. S. A.* **102**, 15757 (2005)  
Y. Huang, S. Joo, M. Duhon, M. Heller, B. Wallace, X. Xu, *Anal. Chem.* **74**, 3362 (2002)  
C. Iliescu, L. Yu, F.E.H. Tay, B. Chen, *Sens. Actuators B Chem.* **129**, 491 (2008)  
C.S. Ivanoff, T.L. Hottel, F. Garcia-Godoy, *Electrophoresis* **33**, 1311 (2012)  
T.B. Jones, *Electromechanics of Particles* (Cambridge University Press, Cambridge, 1995)  
M. Koklu, S. Park, S. D. Pillai, and A. Beskok, *Biomicrofluidics* **4**, (2010).  
P. Kollmannsberger and B. Fabry, *Rev. Sci. Instrum.* **78**, 114301 (2007).  
T.J. Kwak, I. Hossen, R. Bashir, W.-J. Chang, C.H. Lee, *Sci. Rep.* **9**, 18977 (2019a)  
T. J. Kwak, H. Jung, B. D. Allen, M. C. Demirel, and W.-J. Chang, *Sep. Purif. Technol.* **262**, 118280 (2021).  
T.J. Kwak, H. Lee, J.C. Woehl, W.-J. Chang, in, , *IEEE Gt. Lakes Biomed. Conf. GLBC* **2017**, 1–1 (2017)  
T.J. Kwak, J.W. Lee, D.S. Yoon, S.W. Lee, *J. Biomed. Eng. Res.* **34**, 123 (2013)



- T. J. Kwak, M. R. U. Rahman, J. C. Woehl, and W.-J. Chang, in *2019 34th Int. Tech. Conf. CircuitsSystems Comput. Commun. ITC-CSCC* (2019b), pp. 1–3.
- H. Lee, T.J. Kwak, J.C. Woehl, W.-J. Chang, in , IEEE Gt. Lakes Biomed. Conf. GLBC **2017**, 1–1 (2017)
- J. Lee, J.S. Jeong, K.K. Shung, *Ultrasonics* **53**, 249 (2013a)
- J. Lee, T.J. Kwak, D.S. Yoon, S.W. Lee, *J. Biomed. Eng. Res.* **34**, 189 (2013b)
- K. Lee, H. Shao, R. Weissleder, H. Lee, *ACS Nano* **9**, 2321 (2015)
- T. Lilliehorn, U. Simu, M. Nilsson, M. Almqvist, T. Stepinski, T. Laurell, J. Nilsson, S. Johansson, *Ultrasonics* **43**, 293 (2005)
- M. Lombardini, M. Bocchi, L. Rambelli, L. Giulianelli, R. Guerrieri, *Lab. Chip* **10**, 1204 (2010)
- Y.W. Lu, C. Sun, Y.C. Kao, C.L. Hung, J.Y. Juang, *Nanomaterials* **10**, 1364 (2020)
- S. Mahshid, J. Lu, A.A. Abidi, R. Sladek, W.W. Reisner, M.J. Ahamed, *Sci. Rep.* **8**, 5981 (2018)
- N. Malagnino, G. Pesce, A. Sasso, E. Arimondo, *Opt. Commun.* **214**, 15 (2002)
- G.H. Markx, P.A. Dydá, R. Pethig, *J. Biotechnol.* **51**, 175 (1996)
- H. Maruyama, S. Sakuma, Y. Yamanishi, F. Arai, in , IEEEESICE Int. Symp. Syst. Integr. SII **2009**, 7–12 (2009)
- A. Mauro, *Q. Rev. Biol.* **55**, 68 (1980)
- N. Mittal, A. Rosenthal, J. Voldman, *Lab. Chip* **7**, 1146 (2007)
- M. Nakano, Z. Ding, K. Matsuda, J. Xu, M. Inaba, and J. Suehiro, *Biomicrofluidics* **13**, 064109 (2019).
- H.R. Nejad, O.Z. Chowdhury, M.D. Buat, M. Hoorfar, *Lab. Chip* **13**, 1823 (2013)
- I.S. Park, T.J. Kwak, G. Lee, M. Son, J.W. Choi, S. Choi, K. Nam, S.-Y. Lee, W.-J. Chang, K. Eom, D.S. Yoon, S. Lee, R. Bashir, S.W. Lee, *ACS Nano* **10**, 4011 (2016)
- I.S. Park, J. Lee, G. Lee, K. Nam, T. Lee, W.-J. Chang, H. Kim, S.-Y. Lee, J. Seo, D.S. Yoon, S.W. Lee, *Anal. Chem.* **87**, 5914 (2015)
- S. Park, A. Beskok, *Anal. Chem.* **80**, 2832 (2008)
- G. Pesce, G. Volpe, O.M. Maragó, P.H. Jones, S. Gigan, A. Sasso, G. Volpe, *JOSA B* **32**, B84 (2015)
- R. Pethig, *Biomicrofluidics* **4**, 022811 (2010a).
- R. Pethig, *Biomicrofluidics* **4**, (2010b).
- R. Pethig, *Adv. Drug Deliv. Rev.* **65**, 1589 (2013)
- H. A. Pohl, *Camb. Camb. UK* (1978).
- H.A. Pohl, I. Hawk, *Science* **152**, 647 (1966)
- M. Pribyl, D. Snita, and M. Marek, *Model. Simul.* (2008).
- M. Punjiya, H.R. Nejad, J. Mathews, M. Levin, S. Sonkusale, *Sci. Rep.* **9**, 1 (2019)
- M. R. U. Rahman, T. J. Kwak, J. C. Woehl, and W.-J. Chang, *ELECTROPHORESIS* **42**, 644 (2021)
- A. Ramos, H. Morgan, N. G. Green, and A. Castellanos, *J. Colloid Interface Sci.* **217**, (1999).
- A. Sarangan, *Physical and Chemical Vapor Deposition* (Routledge Handbooks Online, 2016).
- M.A. Saucedo-Espinosa, M.M. Rauch, A. LaLonde, B.H. Lapizco-Encinas, *Electrophoresis* **37**, 635 (2016)
- M. L. Y. Sin, V. Gau, J. C. Liao, and P. K. Wong, *JALA Charlottesv. Va* **15**, 426 (2010).
- H. Song and D. J. Bennett, in (American Society of Mechanical Engineers Digital Collection, 2009), pp. 43–50.
- Y. Song, J. Yang, X. Shi, H. Jiang, Y. Wu, R. Peng, Q. Wang, N. Gong, X. Pan, Y. Sun, D. Li, *Sci. China Chem.* **55**, 524 (2012)
- S. Sridharan, J. Zhu, G. Hu, X. Xuan, *Electrophoresis* **32**, 2274 (2011)
- P. Tajik, M.S. Saidi, N. Kashaninejad, N.-T. Nguyen, *Ind. Eng. Chem. Res.* **59**, 3772 (2020)
- B.J. Tauro, D.W. Greening, R.A. Mathias, H. Ji, S. Mathivanan, A.M. Scott, R.J. Simpson, *Methods* **56**, 293 (2012)
- R.S. Thomas, H. Morgan, N.G. Green, *Lab. Chip* **9**, 1534 (2009)
- R.S.W. Thomas, P.D. Mitchell, R.O.C. Oreffo, H. Morgan, N.G. Green, *Electrophoresis* **40**, 2718 (2019)
- G. Volpe, G. Volpe, and D. Petrov, *Phys. Rev. E* **76**, 061118 (2007).
- L. Wang, J. Lu, S.A. Marchenko, E.S. Monuki, L.A. Flanagan, A.P. Lee, *Electrophoresis* **30**, 782 (2009)
- Y. Wang, F. Du, M. Baune, J. Thöming, *Microfluid. Nanofluidics* **17**, 499 (2014)
- P.-Y. Weng, I.-A. Chen, C.-K. Yeh, P.-Y. Chen, and J.-Y. Juang, *Biomicrofluidics* **10**, (2016).
- A. Winkleman, K.L. Gudiksen, D. Ryan, G.M. Whitesides, D. Greenfield, M. Prentiss, *Appl. Phys. Lett.* **85**, 2411 (2004)
- Y. Yan, D. Guo, S. Wen, *BioChip J.* **11**, 196 (2017)
- J. Yang, Y. Huang, X.-B. Wang, F.F. Becker, P.R.C. Gascoyne, *Anal. Chem.* **71**, 911 (1999)

**Publisher's Note** Springer Nature remains neutral with regard to jurisdictional claims in published maps and institutional affiliations.